# Dynamic Detection of Nearby Space Objects with Binary Wide Field of View X-Ray Sensing

Andrea López*, Julian Hammerl†, and Hanspeter Schaub‡
*University of Colorado Boulder, Boulder, CO, 80303*

**Ambient plasma interacts with any object in space and as a result induces the emission of x-rays. A new method of exploiting these interactions for passively detecting objects in the vicinity of a spacecraft is proposed, consisting on a wide field of view x-ray detection solution mounted on a rotating platform. Previous work considered a static target scenario, the heading of which was determined using a batch least squared approach. This work investigates prototypical dynamic scenarios, with the target object following a simple motion with respect to the observer spacecraft. Acquisition/loss of signal events are used in conjunction with a dynamic model of the target motion to obtain the target heading and relative motion by employing a sequential filtering approach. While using the acquisition/loss events directly with a filter is un-observable, a hybrid approach is investigated where the earlier batch solution (assumes static target) is used to get a heading, and this heading observation is then processed through a filter.**

## I. Introduction

Spacecraft in geosynchronous orbit provide a vital communications and surveillance role, but they operate in a domain where defunct spacecraft and debris accumulation are a risk factor, and this region can be difficult to monitor with ground-based systems [1]. Future trends for a sustainable exploitation of this region include in-orbit servicing procedures [2]. Strategic interest in the Moon and cislunar space is growing for private companies and government agencies, with in-orbit assembly and proximity operations being a crucial step in prospective missions[2, 3]. Continuous ground-based monitoring of this region is however not viable. Passive object detection and tracking in the proximity of a spacecraft is an asset for a wide range of applications, including On Orbit Servicing, Assembly and Manufacturing (OSAM), Space Situational Awareness (SSA), and Space Traffic Management (STM). A new method of using ambient plasma-induced x-rays to detect objects in the vicinity of a spacecraft is proposed for GEO orbits and the cislunar region. Commonly, x-ray sensors in space are designed for astronomy applications, with typical fields of view (FOV) of arc-minutes. The purpose of this research in to investigate the development of a wide FOV x-ray sensor of the form of a cluster of off-the-shelf components with a FOV of tens of degrees, capable of detecting objects passively over distances of meters to kilometers.

The x-ray spectrum generated from ambient space environment electrons impacting an object's surface provides the means for detecting the object over a range of distances depending on local plasma properties. Energetic electrons (>1keV) interact with an atomic nucleus through different mechanisms. When an inner shell electron is removed by interaction with the incident electron, the resultant configuration is energetically unstable. An outer shell electron then relaxes to fill the vacancy, and the energy difference between the shells is emitted as characteristic x-rays, with energy that is specific to the element of origin. Solar-induced secondary fluorescence can also excite the release of characteristic x-rays [4]. This characteristic x-ray emission allows for a rapid assessment of an object by spectral signature [5]. A different interaction mechanism occurs when an electron passes close to an atomic nucleus and is slowed down. The energy lost in this interaction is also emitted as an x-ray. Because there are infinite paths for this interaction to take place, the energy loss and therefore the x-ray emission form a continuum, known as the bremsstrahlung radiation. These energetic electrons are present in ambient plasma in regions such as geostationary orbits (GEO) and cislunar space. Bremsstrahlung radiation has been previously used to remotely estimate the electrical potential of an object, utilizing x-ray detectors in combination with an electron gun to excite x-ray emissions of a known target [6, 7].

*PhD Student, Ann and H.J. Smead Department of Aerospace Engineering Sciences, University of Colorado, Boulder, Boulder, CO, 80303. AIAA Member.

†PhD Student, Ann and H.J. Smead Department of Aerospace Engineering Sciences, University of Colorado, Boulder, Boulder, CO, 80303. AIAA Member.

‡Glenn L. Murphy Chair of Engineering, Ann and H.J. Smead Department of Aerospace Engineering Sciences, University of Colorado, Boulder, 431 UCB, Colorado Center for Astrodynamics Research, Boulder, CO, 80303. AAS Fellow, AIAA Fellow.

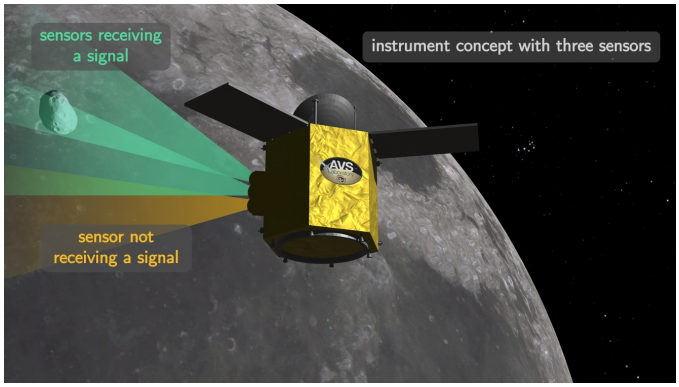


**Fig. 1 Three-sensor instrument concept, with two sensors detecting a nearby object**

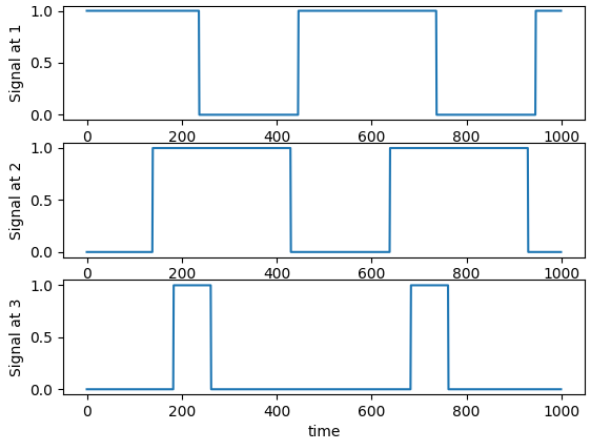


**Fig. 2 Example of signals for a three-sensor instrument concept**

This work investigates the use of a wide FOV x-ray detection solution that exploits the natural space environment interactions to detect and track objects neighboring a spacecraft. The x-ray detection capabilities depend on local plasma properties, but are not contingent on illumination conditions and would potentially present an advantage over visible light detection methods as they will function in the Moon's shadow and Earth's eclipse regions. The proposed sensor consists of a cluster of off-the-shelf x-ray detectors mounted on a rotating platform. A three-sensor instrument concept is shown in Fig. 1. The signal at each detectors is modeled as an on/off step signal, with a value of 1 if the target is visible by the sensor, and 0 otherwise (see Fig. 2). The events of *signal acquisition* and *loss of signal* are used to estimate the heading of the incoming x-ray signal, providing the means to locate the target object passively.

Previous work considered the case of a target that is stationary with respect to the observer spacecraft [8]. Here the acquisition/loss events are modeled as a step function. In this scenario, the acquisition/loss of signal events are generated by the motion of the platform with respect to the spacecraft. The heading estimation in this case is obtained using a deterministic approach, with sensor measurements available at a specific time. The baseline algorithm employed is a batch least squares method. This elegant setup allowed for a discussion of preliminary design trade-offs, comparing a range of configurations for the individual sensors, as well as other design parameters such as FOV of the individual sensors, number of sensors and overlap. The performance of this methodology for obtaining the heading of the target object was analyzed by adding uncertainty in the pointing of the individual sensors in the form of additive white Gaussian noise (AWGN), and comparing the errors in the estimated state with the level of uncertainty. Nevertheless, if only one of the detectors receives a signal from the target, its heading cannot be unequivocally determined, as there are generally two valid solutions to the problem, and the ambiguity cannot be resolved.

However, in a realistic in-orbit scenario, encountering a target with perfectly zero relative motion with respect to

the observer spacecraft is unlikely. But, the relative motion velocities are typically very small, meaning the relative heading will vary slowly. Additionally, although the *a posteriori* batch data processing is useful to characterize the performance of the proposed wide FOV detector and identify feasible design solutions, this approach would present clear disadvantages when employed in a realistic in-orbit application. The present work focuses on expanding the detection and estimation capabilities to a dynamic problem, in which the target object is not stationary, but it follows a simple trajectory with respect to the observer. A sequential filter algorithm is implemented to estimate the heading and relative motion of the target. In contrast with the batch method used in previous work, this approach combines sensor measurements over a continuous range of time with a dynamic model of the target dynamics to estimate its direction and relative motion. A similar approach was followed in Reference [9], using coarse sun sensor measurements to estimate the sun-direction vector. However, the coarse sun sensor based heading estimation was based on having a cosine-like sensor signal, while the presented x-ray based sensing assumes we only measure the acquisition or loss of the x-ray signal at a known field of view angle.

## II. Problem Statement

### A. Sensor configuration and measurements

The sensor configuration used for this work is a single cluster of six x-ray sensors mounted on a rotating platform. The spacecraft body frame is defined as $\mathcal{B} : \{\hat{\boldsymbol{b}}_1, \hat{\boldsymbol{b}}_2, \hat{\boldsymbol{b}}_3\}$. The platform coordinate frame is defined as $\mathcal{P} : \{\hat{\boldsymbol{p}}_1, \hat{\boldsymbol{p}}_2, \hat{\boldsymbol{p}}_3\}$, with $\hat{\boldsymbol{p}}_3 = \hat{\boldsymbol{b}}_3 = \boldsymbol{n}_P$ the unit vector normal to the platform (and normal to the spacecraft surface in which is mounted). The platform is assumed to be rotating with respect to the spacecraft body frame with constant angular velocity $\boldsymbol{\omega}_{P/B} = \omega \boldsymbol{n}_P$.

The FOV of each individual sensor is 15° (half-cone angle). The pointing of the sensors with respect to the platform is defined in azimuth ($\theta$) and elevation ($\phi$) angles, and given in Table 1. Azimuth is measured from the platform positive $\boldsymbol{p}_1$ axis around the $+\boldsymbol{n}_P$ axis, and elevation is measured positive toward the platform $\boldsymbol{n}_P$ axis from the $p_1 p_2$ plane. An illustration of this configuration is shown in Fig. 3.

| Sensor | $\theta$ [deg] | $\phi$ [deg] |
|---|---|---|
| 1 | 0 | 0 |
| 2 | 0 | 15 |
| 3 | 0 | 30 |
| 4 | 0 | 45 |
| 5 | 0 | 60 |
| 6 | 0 | 75 |

**Table 1 Azimuth and elevation angles of x-ray sensors for the configuration used**

This sensor configuration provides a coverage after a full rotation of $2.52\pi$ sr around $\boldsymbol{n}_P$, with a $1.93\pi$ sr ring being covered by at least two sensors (see Fig. 4). For further details on different sensor configurations and visibility and error studies see Reference [8].

In this work, the target is modeled as a point source with a simple trajectory relative to the observer spacecraft. For each of the sensors, the signals are modeled as step functions (see Fig. 2), with a value of 0 when the target is out of the field of view of a sensor, and 1 when the target is within sight of the sensor. The acquisition or loss of signal trigger events are then recorded and can be used to solve for the heading of the target. At the time of a trigger event, the target is at the edge of the field of view of a sensor:

$$\boldsymbol{m}^T \boldsymbol{h} = \cos f \tag{1}$$

where $\boldsymbol{m}$ is the unit vector of the pointing of the pertinent sensor, $\boldsymbol{h}$ is the unit heading of the target object, and $f$ is the half angle of the field of view cone.

In previous work, for a target assumed stationary with respect to the observer spacecraft, a combination of multiple trigger events with this simplified model of the signal behavior is enough to obtain an accurate heading for the target

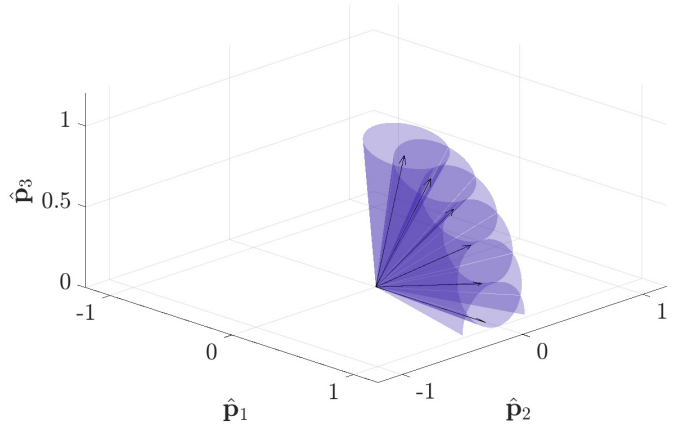


**Fig. 3 Illustration of sensor configuration with respect to platform frame of reference**

object:

$$\begin{bmatrix} \boldsymbol{m}_1^T \\ \boldsymbol{m}_2^T \\ \dots \\ \boldsymbol{m}_p^T \end{bmatrix} \boldsymbol{h} = \begin{bmatrix} \cos f \\ \cos f \\ \dots \\ \cos f \end{bmatrix} \tag{2}$$

with $\boldsymbol{m}_j$ the $j^{\text{th}}$ measurement obtained from any of the sensors and $p$ the total number of measurements considered. The measurement equation is then in the classic matrix-vector form $M\boldsymbol{x} = \boldsymbol{y}$.

### B. Observability study

For this work, the system is modeled in state-space representation as a time-invariant linear system with no control inputs

$$\begin{cases} \dot{\boldsymbol{x}}(t) = A\boldsymbol{x}(t) \\ \boldsymbol{y}(t) = C\boldsymbol{x}(t) \end{cases} \tag{3}$$

In this simple case, the observability of the system is tested by checking the rank of the observability matrix $O$

$$O = \begin{bmatrix} C \\ CA \\ CA^2 \\ \vdots \\ CA^{n-1} \end{bmatrix} \tag{4}$$

where $n$ is the number of variables in the state vector. If $\text{rank}(O) = n$, the system is observable.

Three different dynamic models are considered for this analysis: a double-integrator system, a Clohessy-Wiltshire system, and a constant angular rate system.

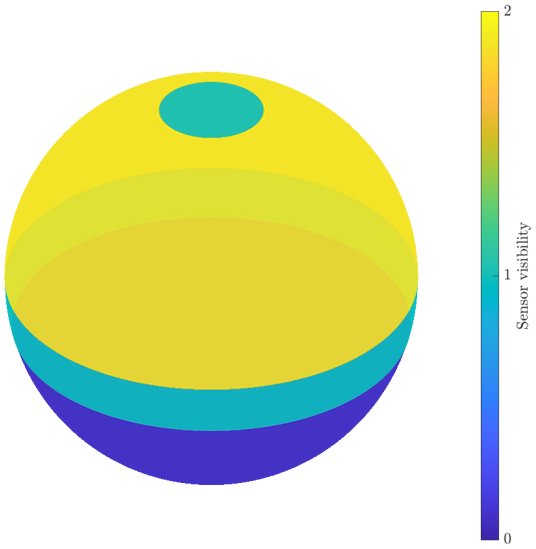


**Fig. 4 Visibility map on a unit sphere for the given configuration**

*1. Double Integrator Dynamics*

For this case, the target is moving at a constant velocity with respect to the observer spacecraft. The state vector is

$$\boldsymbol{x}(t) = \begin{bmatrix} \boldsymbol{r}(t) \\ \dot{\boldsymbol{r}}(t) \end{bmatrix} \tag{5}$$

where $\boldsymbol{r}(t)$ and $\dot{\boldsymbol{r}}(t)$ are the observer-target position and velocity vectors respectively. The dynamics equation is then

$$\dot{\boldsymbol{x}}(t) = A\boldsymbol{x}(t) = \begin{bmatrix} \bar{0}_{3\times3} & \mathbb{I}_{3\times3} \\ \bar{0}_{3\times3} & \bar{0}_{3\times3} \end{bmatrix} \boldsymbol{x}(t) \tag{6}$$

When considering a single trigger event, the measurement equation at the time of the event becomes

$$\boldsymbol{y}(t) = C\boldsymbol{x}(t) = \begin{bmatrix} \boldsymbol{m}(t)^T & \bar{0}_{1\times3} \end{bmatrix} \boldsymbol{x}(t) = r\cos f \tag{7}$$

where $\boldsymbol{m}(t)$ is the pointing of the sensor recording the event at time $t$, $r$ the magnitude of the position vector (assumed known for the purpose of this analysis) and $f$ the half-cone angle of the FOV of the sensor.

The observability matrix obtained in this case has $\text{rank}(\mathcal{O}) = 2 < n = 6$, and the problem is not observable.

*2. Clohessy-Wiltshire equations*

Using the Clohessy-Wiltshire [10] equations to describe the motion of the target with respect to the observer, with the same state vector as in the previous case, the dynamics equation is

$$\dot{\boldsymbol{x}}(t) = A\boldsymbol{x}(t) = \begin{bmatrix} 0 & 0 & 0 & 1 & 0 & 0 \\ 0 & 0 & 0 & 0 & 1 & 0 \\ 0 & 0 & 0 & 0 & 0 & 1 \\ 3n^2 & 0 & 0 & 0 & 2n & 0 \\ 0 & 0 & 0 & -2n & 0 & 0 \\ 0 & 0 & -n^2 & 0 & 0 & 0 \end{bmatrix} \boldsymbol{x}(t) \tag{8}$$

with $n$ the mean motion of the observer, assumed to be in a circular orbit.

Using the same measurement equation as in the previous case, the resulting observability matrix is $\text{rank}(\mathcal{O}) = 4 < n = 6$, and the system is not observable.

*3. Constant angular rate dynamics*

For this case, the state vector is defined as

$$\boldsymbol{x}(t) = \begin{bmatrix} \boldsymbol{h}(t) \\ \dot{\boldsymbol{h}}(t) \end{bmatrix} \tag{9}$$

where $\boldsymbol{h}(t)$ and $\dot{\boldsymbol{h}}(t)$ are the heading and heading rate of the target with respect to the observer, respectively. Note that $\boldsymbol{h} = \boldsymbol{r}/r$. The motion considered here is defined by a constant angular rate $\boldsymbol{\omega}$ perpendicular to the heading vector, such that $\dot{\boldsymbol{h}}(t) = \boldsymbol{\omega} \times \boldsymbol{h}(t)$ and $\ddot{\boldsymbol{h}}(t) = \boldsymbol{\omega} \times (\boldsymbol{\omega} \times \boldsymbol{h}(t))$.

The dynamics equation is then

$$\dot{\boldsymbol{x}}(t) = A\boldsymbol{x}(t) = \begin{bmatrix} [\boldsymbol{\omega}]_\times & \mathbb{I}_{3\times3} \\ [\boldsymbol{\omega}]_\times^2 & [\boldsymbol{\omega}]_\times \end{bmatrix} \boldsymbol{x}(t) \tag{10}$$

where $[\cdot]_\times$ represents the skew-symmetric cross product matrix given by

$$\boldsymbol{a} = \begin{bmatrix} a_1 \\ a_2 \\ a_3 \end{bmatrix}, \quad [\boldsymbol{a}]_\times = \begin{bmatrix} 0 & -a_3 & a_2 \\ a_3 & 0 & -a_1 \\ -a_2 & a_1 & 0 \end{bmatrix}.$$

Using a similar measurement equation as in the previous cases,

$$\boldsymbol{y}(t) = C\boldsymbol{x}(t) = \begin{bmatrix} \boldsymbol{m}(t)^T & \bar{0}_{1\times3} \end{bmatrix} \boldsymbol{x}(t) = \cos f \tag{11}$$

The resulting observability matrix for this model has $rank(\mathcal{O}) = 4 < n = 6$, and the system is not observable.

*Conclusion*

The result from the analysis of these three cases motivated the utilization of intermediate heading measurements, obtained by batch-processing a group of trigger events, instead of using a single trigger event as a measurement. By doing this, the output matrix $C$ is of the form

$$\boldsymbol{y}(t) = C\boldsymbol{x}(t) = \begin{bmatrix} \mathbb{I}_{3\times3} \bar{0}_{3\times3} \end{bmatrix} \boldsymbol{x}(t) \tag{12}$$

and the observability matrices for all three cases become full rank (rank$(\mathcal{O}) = 6 = n$).

### C. Measurement pre-processing

The previous section justifies the use of full heading estimations for this tracking problem in lieu of single trigger events obtained directly from the sensors. This requires an intermediate step of clustering enough trigger events together such that an accurate heading estimation can be obtained.

With the configuration described in Section II.A, most of the field of view of the instrument is covered by overlapping sensors. From Reference [8], at least three unique trigger events are needed to unequivocally estimate a heading. For a target moving slowly with respect to the rotation of the instrument platform, most cases yield four trigger events from the overlapping sensors: an "on" trigger and an "off" trigger from each of the two sensors.

An algorithm was developed such that the trigger events are grouped by proximity in time, and the groups with 3 or more measurements are used to obtain heading estimates. This algorithm is based on the pairwise distance matrix $D$, where each element of $D$, $d_{ij}$, is the time euclidean distance between two trigger events $i$ and $j$:

$$D = [d_{ij}], \quad d_{ij} = \sqrt{t_i^2 - t_j^2} \tag{13}$$

Two measurements belong to the same group if $d_{ij} < g$, where $g$ is a gating threshold. This gate value was decided *ad hoc*, based on the fact that typically no more than four trigger events will be grouped together. The gate used $g$ is the average of all $g_i$ values obtained, where

$$g_i = \frac{\sum_{k=0}^{4} d_{i+k,i}}{5}, \quad i = 1, ..., n-4 \tag{14}$$

Where $n$ is the total number of trigger events considered. Each resulting cluster contains either one, two, three or four trigger events. The clusters with three and four trigger events are used to obtain heading measurements, from Eq. 2 with $p = 3$ and $p = 4$ respectively. The estimated heading is

$$\boldsymbol{h} = M^{+} \begin{bmatrix} \cos f \\ \dots \\ \cos f \end{bmatrix} \tag{15}$$

where $M^{+}$ is the Moore-Penrose inverse of matrix $M$.

The time associated with the heading measurement is then the average time of the trigger events considered. Figure 5 illustrates the heading measurements obtained from a series of trigger events for an arbitrary constant-velocity trajectory of the target. In this example, the sensor platform is rotating with $\omega = 10°/s$ and the sampling frequency is 10 Hz.

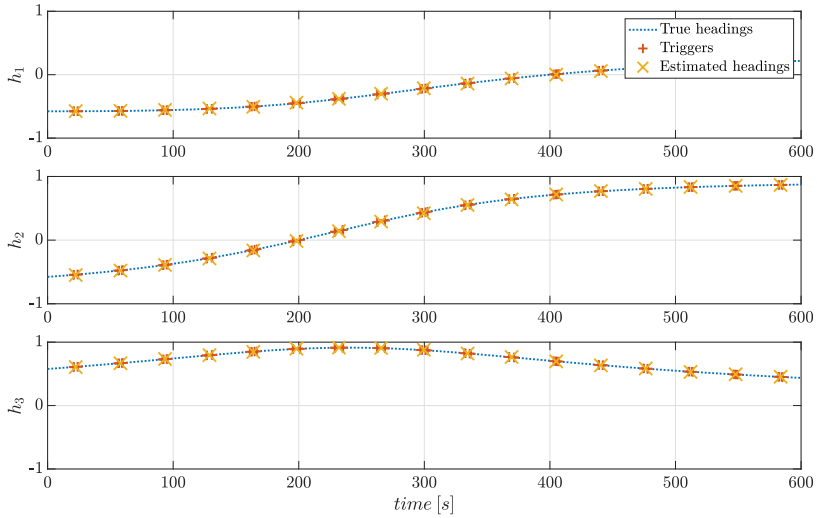


**Fig. 5 Example of trigger locations and heading estimations for an arbitrary target trajectory**

## III. Sequential Filtering

### A. Linear Kalman Filter

Instead of solving the geometry of the sensor measurements at an instant in time, heading measurements are used to correct a propagated target heading estimate. This section describes the application of a linear Kalman filter to the problem of estimating the heading and heading rates of a target object. The reader is referred to References [11–14] for more information on the Kalman filter and its equations.

The state vector considered in this problem is

$$\boldsymbol{x}(t) = \begin{bmatrix} \boldsymbol{h}(t) \\ \dot{\boldsymbol{h}}(t) \end{bmatrix} \tag{16}$$

where $\boldsymbol{h}(t)$ and $\dot{\boldsymbol{h}}(t)$ are the heading and heading rate of the target object being tracked.

A simplified state transition model is used in this linear Kalman filter implementation, assuming a double integrator model with

$$\dot{\boldsymbol{x}}(t) = A\boldsymbol{x}(t) + B_w \boldsymbol{w}(t) = \begin{bmatrix} \bar{0}_{3\times3} & \mathbb{I}_{3\times3} \\ \bar{0}_{3\times3} & \bar{0}_{3\times3} \end{bmatrix} \boldsymbol{x}(t) + \begin{bmatrix} \bar{0}_{3\times3} \\ \mathbb{I}_{3\times3} \end{bmatrix} \boldsymbol{w}(t) \tag{17}$$

where $\boldsymbol{w}(t)$ is the process noise that accounts for the uncertainty in the dynamics model, modeled as $\boldsymbol{w}(t) \sim \mathcal{N}(\bar{0}, Q(t))$.

The state vector can be expressed in discrete time $t_k$ as a function of the state at the previous time step $t_{k-1}$ and the state transition matrix (STM) as

$$\boldsymbol{x}_k = \Phi(t_k, t_{k-1})\boldsymbol{x}_{k-1} + \boldsymbol{w}_k \tag{18}$$

where $\boldsymbol{w}_k$ is the process noise in discrete time, and $\boldsymbol{w}_k \sim \mathcal{N}(\bar{0}, Q_{t_k,t_{k-1}})$.

For this linear time invariant (LTI) system, the state transition matrix takes the simple form

$$\Phi(t_k, t_{k-1}) = \exp\{A(t_k - t_{k-1})\} = \begin{bmatrix} \mathbb{I}_{3\times3} & \mathbb{I}_{3\times3}(t_k - t_{k-1}) \\ \bar{0}_{3\times3} & \mathbb{I}_{3\times3} \end{bmatrix} \tag{19}$$

The discrete-time covariance of the process noise is

$$Q_{t_k,t_{k-1}} = \int_{t_{k-1}}^{t_k} \Phi(t_k, \tau) B_w Q B_w^T \Phi(t_k, \tau)^T d\tau = \begin{bmatrix} \frac{1}{3}Q\mathbb{I}_{3\times3}(t_k - t_{k-1})^3 & \frac{1}{2}Q\mathbb{I}_{3\times3}(t_k - t_{k-1})^2 \\ \frac{1}{2}Q\mathbb{I}_{3\times3}(t_k - t_{k-1})^2 & Q\mathbb{I}_{3\times3}(t_k - t_{k-1}) \end{bmatrix} \tag{20}$$

The measurement equation used, in discrete time, is

$$\boldsymbol{y}_k = H\boldsymbol{x}_k + \boldsymbol{v}_k = \begin{bmatrix} \mathbb{I}_{3\times3} & \bar{0}_{3\times3} \end{bmatrix} \boldsymbol{x}_k + \boldsymbol{v}_k \tag{21}$$

where $\boldsymbol{v}_k$ is the measurement noise modeled as $\boldsymbol{v}_k \sim \mathcal{N}(\bar{0}, R_k)$. The measurement covariance is $R_k = \sigma_k^2 \mathbb{I}_{3\times3}$, where $\sigma_k^2$ is the variance of the measurement noise. The measurements $\boldsymbol{y}_k$ are the heading estimates obtained with the batch pre-processing described in Section II.C.

Because the state vector consists of heading and heading rates, there are geometric constraints that these vectors need to satisfy. These constraints, enforced at every time step, are $|\boldsymbol{h}| = h = 1$ and $\boldsymbol{h}^T\dot{\boldsymbol{h}} = 0$. Therefore,

$$\begin{cases} \hat{\boldsymbol{h}}_k = \frac{\hat{\boldsymbol{h}}_k}{|\hat{\boldsymbol{h}}_k|} \\ \dot{\hat{\boldsymbol{h}}}_k = \dot{\hat{\boldsymbol{h}}}_k - \hat{\boldsymbol{h}}_k^T \dot{\hat{\boldsymbol{h}}}_k \end{cases} \tag{22}$$

where $\hat{\boldsymbol{h}}_k$ and $\dot{\hat{\boldsymbol{h}}}_k$ are the best estimates of the heading and heading rate at time $t_k$.

### B. Results

A simple arbitrary constant-velocity target trajectory was simulated, and the described implementation was used to detect and track the target object. The results of that process are shown in this section.

The initial conditions of the target are ${}^{\mathcal{B}}\boldsymbol{r}_0^T = [-100 \quad -100 \quad 100]$ and ${}^{\mathcal{B}}\dot{\boldsymbol{r}}_0^T = [0.25 \quad 0.5 \quad 0]$, given in m and m/s respectively. These position and velocity vectors are expressed in the observer body frame $\mathcal{B} : \{\hat{\boldsymbol{b}}_1, \hat{\boldsymbol{b}}_2, \hat{\boldsymbol{b}}_3\}$. This trajectory is propagated for 10 minutes and the corresponding trigger events are obtained, with the platform rotating at $\omega = 10°/\text{s}$ and a sampling frequency of 10 Hz.

The filter is initiated at the time of the first heading batch estimation (in this example, $t_1 = 22.4$ s, $\boldsymbol{h}_1^T \approx [-0.5741 \quad -0.5491 \quad 0.6073]$). The *a priori* state vector given to the filter is

$$\boldsymbol{x}_0 = \begin{bmatrix} \boldsymbol{h}_1 \\ \bar{0}_{3\times1} \end{bmatrix} \tag{23}$$

The *a priori* state covariance used is $P_0 = \text{diag}([1 \quad 1 \quad 1 \quad 0.01 \quad 0.01 \quad 0.01])$. The filter is initiated with process noise $Q = 1 \cdot 10^{-6}$ and measurement standard deviation $\sigma_k = 1$. The results from the linear Kalman filter are shown in Figs. 6-8.

The error in heading estimation, defined as $\Delta\boldsymbol{h} = \boldsymbol{h}_{\text{truth}} - \hat{\boldsymbol{h}}$, and heading rate, defined as $\Delta\dot{\boldsymbol{h}} = \dot{\boldsymbol{h}}_{\text{truth}} - \dot{\hat{\boldsymbol{h}}}$, are shown in Figs. 6 and 7, respectively. The effect of the added process noise, the increased uncertainty in the propagated states between measurements, is visible there. Figure 8 shows the evolution of the magnitude of the heading error and heading rate error vectors. In order to facilitate the interpretation of these results, the angular error (i.e., the angle $\epsilon$ between the true heading and the estimated heading) is shown in Fig. 9.

Note that, for heading and heading rate, the filter dynamics model is not an accurate representation of the motion of the target, and therefore a deviation from the true state was as expected in between measurements. However, the goal of this work is not to correctly model the relative dynamics between two objects in orbit, but to demonstrate a novel approach for utilizing very simple trigger events from x-ray sensors to track a target object.

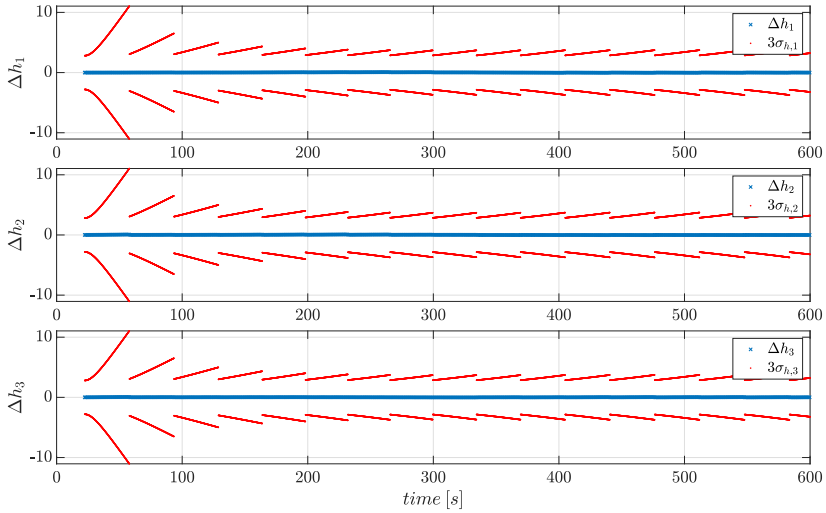


**Fig. 6 Errors in heading estimation components with $3\sigma$ bounds**

## IV. Conclusions

This work investigates the utilization of simple x-ray sensors to passively detect an object in the vicinity of an observer spacecraft, exploiting the natural plasma interactions in the space environment that cause the emission of x-rays. The scope of this paper is to expand previous work (Reference [8]) for cases in which the target object is moving with respect to the observer spacecraft.

A brief discussion of the problem observability confirmed that single trigger events from the sensors cannot be used individually as measurements. An algorithm was then developed to pre-process trigger events by grouping them in clusters (typically with four triggers per cluster), allowing to obtain heading estimates that are then used as measurements in the following steps. The type of sensor configuration used, in which most of the field of view is covered by two overlapping sensors, proved beneficial in obtaining and grouping trigger events for this pre-processing step.

A linear Kalman filter was then implemented to obtain and propagate the heading and heading rate estimates of the target object. An example of results obtained for an arbitrary target trajectory is shown as a proof of concept of the developed approach.

## References

[1] Lal, B., Balakrishnan, A., Caldwell, B. M., Buenconsejo, R. S., and Carioscia, S. A., "Global Trends in Space Situational Awareness (SSA) and Space Traffic Management (STM)," *Institute for Defense Analyses Science & Technology Policy Institute*, 2018.

[2] Corbin, B. A., Abdurrezak, A., Newell, L. P., Roesler, G. M., and Lal, B., "Global Trends in On Orbit Servicing, Assembly and Manufacturing (OSAM)," *Institute for Defense Analyses Science & Technology Policy Institute*, 2020.

[3] Kaplan, S., "Eyes on the Prize. The Strategic Implications of Cislunar Space and the Moon," 2020, p. 4.

[4] Kamata, Y., Takeshima, T., Okada, T., and Terada, K., "Detection of x-ray fluorescence line feature from the lunar surface," *Advances in Space Research*, Vol. 23, No. 11, 1999, pp. 1829–1832.

[5] Wilson, K. T., Bengtson, M. T., and Schaub, H., "X-ray Spectroscopic Determination of Electrostatic Potential and Material Composition for Spacecraft: Experimental Results," *Space Weather*, Vol. 18, No. 4, 2020, p. e2019SW002342.

[6] Hammerl, J., Romero-Calvo, Á., López, A., and Schaub, H., "Touchless potential sensing of complex differentially-charged shapes using X-rays," *AIAA SciTech 2022 Forum*, 2022, p. 2312.

[7] Wilson, K. T., and Schaub, H., "An X-Ray Spectroscopic Approach to Remote Space Object Potential Determination: Experimental Results," *AIAA Scitech 2020 Forum*, 2020, p. 0049.

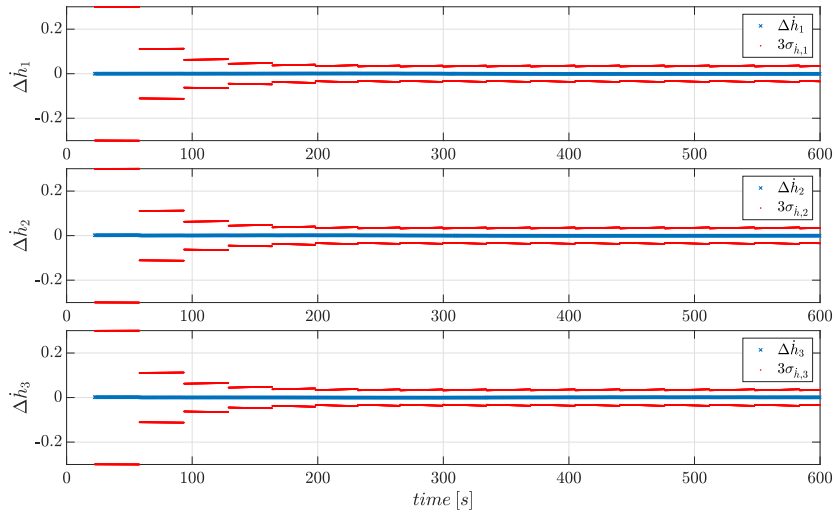


**Fig. 7 Errors in heading rate estimation components with $3\sigma$ bounds**

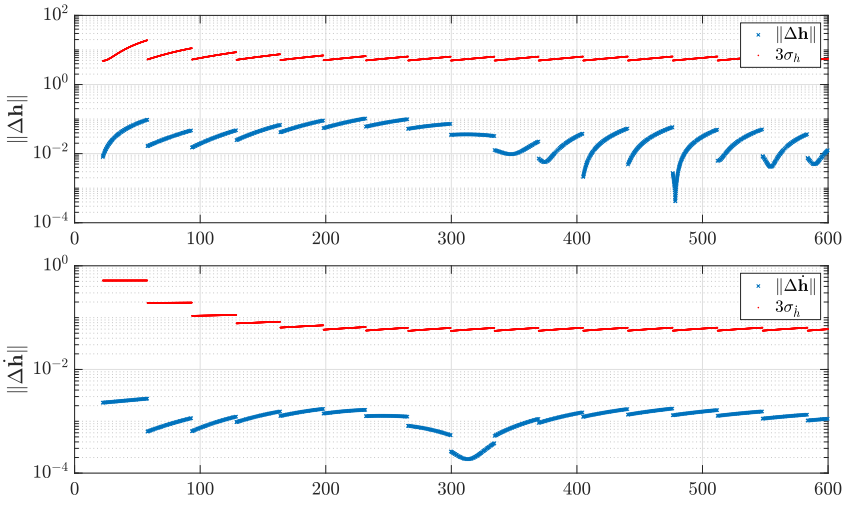


**Fig. 8 Magnitude of the error vectors in heading and heading rate estimation, with $3\sigma$ bounds**

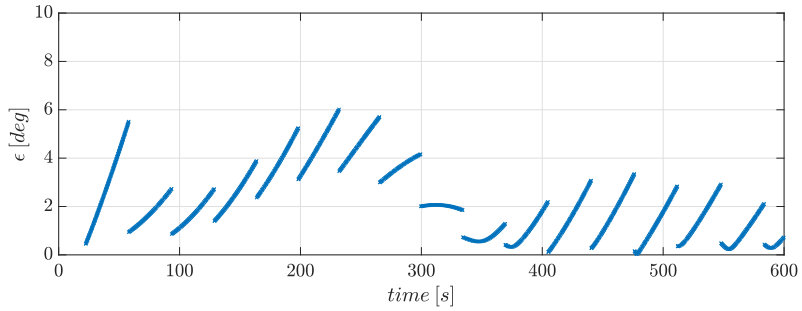


**Fig. 9 Angular error between true and estimated heading**

[8] López, A., Hammerl, J., and Schaub, H., "Detecting Space Objects With Binary Wide Field Of View X-Ray Sensing," *AAS Astrodynamics Specialist Conference*, Charlotte, NC, 2022. Paper No. AAS 22-602.

[9] O'Keefe, S. A., and Schaub, H., "Sun-direction estimation using a partially underdetermined set of coarse sun sensors," *The Journal of the Astronautical Sciences*, Vol. 61, No. 1, 2014, pp. 85–106.

[10] Clohessy, W., and Wiltshire, R., "Terminal guidance system for satellite rendezvous," *Journal of the Aerospace Sciences*, Vol. 27, No. 9, 1960, pp. 653–658.

[11] Kalman, R. E., "A new approach to linear filtering and prediction problems," 1960.

[12] Sorenson, H. W., "Least-squares estimation: from Gauss to Kalman," *IEEE spectrum*, Vol. 7, No. 7, 1970, pp. 63–68.

[13] Brown, R. G., and Hwang, P. Y. C., *Introduction to random signals and applied Kalman filtering: with MATLAB exercises and solutions; 3rd ed.*, Wiley, New York, NY, 1997.

[14] Meinhold, R. J., and Singpurwalla, N. D., "Understanding the Kalman filter," *The American Statistician*, Vol. 37, No. 2, 1983, pp. 123–127.